Dissection of brain-wide spontaneous and functional somatosensory circuits by fMRI with optogenetic silencing

Won Beom Jung[a], Haiyan Jiang[a,b], Soohyun Lee[c], and Seong-Gi Kim[a,b,d *]

[a] Center for Neuroscience Imaging Research (CNIR), Institute for Basic Science (IBS), Suwon 16419, Republic of Korea

[b] Department of Biomedical Engineering, Sungkyunkwan University, Suwon, 16419, Republic of Korea

[c] Unit on Functional Neural Circuits, National Institutes of Health, Bethesda, MD 20892, USA

[d] Department of Intelligent Precision Healthcare Convergence, Sungkyunkwan University, Suwon, 16419, Republic of Korea

***Corresponding author:**

Seong-Gi Kim, IBS Center for Neuroscience Imaging Research, N Center

Sungkyunkwan University, Suwon 16419, Republic of Korea.

Email: seonggikim@skku.edu

Phone number: +82-31-299-4350

Author Contributions: W.B.J. and S.G.K. conceived and planned the experiments; W.B.J. and H.J. performed the experiments; W.B.J. analyzed the data; S.L. provided critical discussion and insights; and W.B.J., S.L. and S.G.K. wrote the manuscript.

Competing Interest Statement: The authors declare no competing interests.

Keywords: fMRI, somatosensory network, optogenetics, neuronal inhibition, circuit dissection, spontaneous activity, resting-sate connectivity

This file includes:

Main Text

Figures 1 to 6

Abstract

To further advance functional magnetic resonance imaging (fMRI)-based brain science, it is critical to dissect fMRI activities at a circuit level. To solve this issue, we propose to combine brain-wide fMRI with neuronal silencing in well-defined regions via temporally specific optogenetic stimulation. Since focal inactivation suppresses excitatory output to downstream pathways, intact input and downregulated output circuits can be separated. Highly specific cerebral blood volume-weighted fMRI was performed with optogenetic simulation of local GABAergic neurons in mouse somatosensory regions at 15.2 T. Brain-wide spontaneous somatosensory networks were found mostly in ipsilateral cortical and subcortical areas, which differ from the bilateral homotopic connections commonly observed in resting-state fMRI. Evoked fMRI response to somatosensory stimulation were dissected to spinothalamic, thalamocortical (TC), corticothalamic (CT), corticocortical (CC) inputs and local intracortical circuits. The primary somatosensory cortex (S1) receives TC inputs from the ventral posterior thalamic nucleus with spinothalamic inputs. The primary motor cortex (M1) has feedforward CC inputs from S1, and the posterior medial thalamic nucleus also receives CT inputs from S1. The secondary somatosensory cortex (S2) receives mostly direct CC inputs from S1 and a small amount of TC inputs. The TC and CC input layers in cortical regions were identified by laminar-specific fMRI responses. The long-range synaptic input in cortical areas is amplified approximately 2-fold by local intracortical circuits, which is consistent with electrophysiological recordings. Overall, whole-brain fMRI with optogenetic inactivation provides brain-wide, population-based long-range circuits, which will complement conventional microscopic functional circuit studies.

Introduction

Functional magnetic resonance imaging (fMRI) has advanced brain science tremendously by noninvasively mapping both functional regions with various stimuli and resting-state functional connectivity. Evoked-fMRI detects the strength of the hemodynamic response to external stimuli (1-3), whereas resting-state fMRI (rs-fMRI) measures the degree of synchrony between fMRI time series among anatomically distinct regions at rest (4-7). Both evoked and resting-state functional networks contain multiple brain regions that are hierarchically yet reciprocally connected via ascending thalamocortical (TC), descending corticothalamic (CT), corticocortical (CC) and intracortical (IC) circuits (8). Therefore, it is critical to determine the relative contributions of different circuits to fMRI findings to better understand brain functions and resting-state connectivity.

To identify the contributions of neural networks to fMRI responses, we propose to silence neural activity in well-defined regions via temporally specific optogenetic control of a given neural population (9). Inhibiting one cortical region inevitably suppresses excitatory output to downstream signaling pathways (e.g., CT, CC, and IC pathways) (10-12), and the downregulated neuronal activity reflects the degree of interregional communication under basal conditions (12). Therefore, fMRI with cortical inactivation is beneficial for brain-wide mapping of functional connectivity in the resting state. Similarly, local silencing during exposure to external stimuli suppresses downstream activity (output-related circuits) without compromising the upstream and/or collateral inputs from other brain regions (input-related circuits) (11, 13-16); thus, the downstream circuit contributions to fMRI can be determined by comparing evoked fMRI response with and without focal inactivation.

In the current study, we adopted a widely investigated somatosensory network involving multiple brain regions, such as the first-order ventral posterior thalamic nucleus, higher-order posterior medial thalamic nucleus (POm), primary somatosensory cortex (S1), secondary somatosensory cortex (S2), and primary motor cortex (M1) (17, 18). Anatomical tracing studies demonstrated the existence of complex mono-synaptic networks across broad somatosensory-related brain areas (19-21). Microscopic

functional circuits in preselected areas have been delineated using electrophysiology (22-26) and optical recordings (27, 28) combined with optogenetic and chemogenetic tools. Recently, macroscopic functional activity in the whole brain was mapped by fMRI (29-32). Thus, the somatosensory system is an ideal model for investigating whether the contributions of different projections to fMRI responses can be separated.

To dissect spontaneous and sensory-evoked fMRI signals at the circuit level, we combined highly specific cerebral blood volume (CBV)-weighted fMRI at ultrahigh magnetic field strength of 15.2 T with optogenetic stimulation of local GABAergic neurons using the VGAT-ChR2-EYFP transgenic mouse line (33). We examined how different cortical areas, including the primary somatosensory forelimb (S1FL), M1 and S2, affect activity in cortical and subcortical brain regions to determine causal relationships in the information flow among multiple brain areas.

Materials and Methods

Animal preparation

All experiments under anesthesia were performed according to the guidelines and with the approval of the Institutional Animal Care and Use Committee of Sungkyunkwan University in accordance with the standards for humane animal care from the Animal Welfare Act and the National Institutes of Health Guide for the Care and Use of Laboratory Animals. A total of 39 mice were used in five different studies: 1) 22 transgenic mice for fMRI with cortical inactivation (VGAT-ChR2-EYFP, n = 8 for S1FL, n = 7 for M1, and n =7 for S2), 2) 6 transgenic mice for electrophysiology recording, 3) 3 naïve mice for contrast agent dose-dependent MRI to optimize the CBV-weighted fMRI protocol (C57BL/6; Orient Bio, Seongnam, Korea), 4) 3 naïve mice for the fMRI study on light-induced heating effects, and 5) 5 naïve mice for conventional resting-state CBV-weighted fMRI. The VGAT-ChR2-EYFP (B6.Cg-Tg (Slc32a1-COP4*H134R/EYFP) 8Gfng/J) mice were bred in-house from breeding pairs obtained from Jackson Laboratory (Bar Harbor, ME, USA). Animals were housed in independently ventilated cages under controlled temperature and humidity conditions and a 12-hour dark-light cycle.

For optogenetic fMRI, fiber-optic cannulas (Thorlabs, Newton, New Jersey, USA) were implanted in mice (VGAT-ChR2-EYFP, n=22; C57BL/6, n=3) at 6-7 weeks of age using a stereotactic surgical procedure (34). In short, the mice were anesthetized by an intraperitoneal (IP) bolus injection of a ketamine and xylazine mixture (100 mg/kg and 10 mg/kg, respectively) and fixed in a stereotaxic frame (SR-AM, Narishige, Tokyo, Japan) for surgery. Meloxicam (1 mg/kg) was administered subcutaneously to provide pain relief and reduce inflammation. After an incision was made on the scalp, the skull was completely washed and dried. The skull was then thinned over the target area to make a burr hole (~ 100 μm diameter) for fiber implantation. The optical fiber cannula (105 μm inner core diameter, NA = 0.22) was then inserted slowly into the right S1FL (AP: - 0.2 mm relative to the bregma, ML: + 2.2 mm and DV: + 0.5 mm relative to the surface), M1 (AP: + 0.05 mm, ML: + 1.1 mm and DV: + 0.25 mm) and S2 (AP: - 1.1 mm, ML: + 3.8 mm and DV: + 0.9 mm) areas through the burr hole at a rate of 1

μm/sec via a micromanipulator (SMX-model, Sensapex, Oulu, Finland). With the fiber-optic implant in place, a biocompatible silicone elastomer (Kwik-Sil, World Precision Instruments, Sarasota, FL, USA) was applied to enclose the fiber implantation site, and dental cement (SB, Sun-Medical Co., Shiga, Japan) was then applied to thinly cover the area around the fiber cannula to fix it onto the skull. After a recovery period of at least 2 weeks, the mice underwent optogenetic fMRI experiments.

The functional experimental procedure was previously described in detail (30, 35). In short, mice were anesthetized using a mixture of ketamine (Yuhan, Korea) and xylazine (Rompun®, Bayer, Korea) (100/10 mg/kg for initial IP, and 25/1.25 mg/kg intermittent IP injections every 45-50 mins) under self-breathing through a nose cone with a continuous supply of oxygen and air (1:4 ratio) at a rate of 1 liter/min (SAR-1000, CWE, Ardmore, USA or TOPO, Kent Scientific Corporation, Torrington, CT, USA) to maintain an oxygen saturation level of > 90%. During the experiments, electrocardiograms and motion-sensitive respiratory signals were continuously monitored (Model 1030, Small Animal Instruments Inc., Stony Brook, USA for fMRI and PhysioSuite, Kent Scientific Corp, USA for electrophysiology studies), and body temperature was maintained at 37 ± 0.5°C with a warm-water heating system and a rectal thermometer.

Stimulation

The stimulation parameters were controlled by a pulse generator (Master 9; World Precision Instruments, Sarasota, FL, USA). For light stimulation, blue light was delivered to the target cortex via a fiber-optic cable coupled to a 473-nm diode-pumped solid-state laser (MBL-III-473, Changchun New Industries Optoelectronics Tech. Co., Ltd, Changchun, China). The constant output power was calibrated to be 3 mW at the tip of the optic fiber, measured by a power meter (PM100D, Thorlabs, USA). Light stimulation was then applied at 20 Hz with a pulse width of 10 ms via a 105 μm diameter fiber. This experimental setting leads to a time-averaged light power of 69.3 mW/mm^2, which is below

the range that generates light-induced artifactual responses (36, 37). To block undesired activation of the visual pathway by light leakage inside the magnet bore, the connection between the fiber optic cable and the implanted cannula was covered with heat-shrinkable sleeves, and the eyes of the animal were covered with a biocompatible silicone elastomer. For somatosensory stimulation, the left forepaw of the mice was electrically stimulated. A pair of needle electrodes (30 G) were inserted under the plantar skin of the forepaw, and electrical pulse stimuli with a current intensity of 0.5 mA (ISO-Flex, AMPI, Jerusalem, Israel), pulse width of 0.5 ms, and frequency of 4 Hz were triggered by a pulse generator (35). Each functional trial consisted of a 60-s (30 s for electrophysiology) prestimulus, 20-s stimulus, 60-s interstimulus, 20-s stimulus, and 60-s (30 s for electrophysiology) poststimulus period.

Electrophysiology

Multiunit activity and local field potential were measured in S1FL to confirm the suppression of neuronal activity during optogenetic cortical inactivation and to investigate the neural source of fMRI findings concerning long-range TC input and local recurrent activity (VGAT-ChR2-EYFP, n = 6). The head was fixed in a stereotaxic frame (SR-10R-HT, Narishige, Tokyo, Japan), and the scalp was removed to expose the skull. After cleaning the skull, two holes (> 0.3 mm diameter) were made with a dental drill to implant the stainless-steel screws for the ground and reference wires. Craniotomy was performed over the right somatosensory area, with a diameter of ~2 mm. CBV-weighted optical imaging (Imager 3001, Optical Imaging Ltd., Rehovot, Israel) of the response to left forepaw stimulation was performed to precisely determine the S1FL area. To simultaneously record neural activities during optogenetic stimulation, a 16-channel opto-electrode with 50 μm spacing between channels (A1x16-5mm-50-177-OA16LP, NeuroNexus, Ann Arbor, MI, USA) was placed at the center of the predefined S1FL and slowly inserted at a speed of 1 μm/sec. During insertion, the electrode was held for 5 mins every 100 μm and for 10 mins when the tip of the electrode reached a cortical depth of ~1 mm to stabilize the position. Electrophysiological signals were measured at a sampling rate of 30 kHz using a

Blackrock Cerebus recording system (Blackrock Microsystems, Salt Lake City, Utah). Functional studies were interleaved across 3 different stimulus paradigms, and 5-8 trials were performed for each experimental condition for each animal.

MRI experiments

All MRI experiments were performed on a 15.2 T MRI scanner with an actively shielded 6-cm diameter gradient operating with a maximum strength of 100 G/cm and a rise time of 110 μs (Bruker BioSpec, Billerica, MA, USA). A 15 mm ID customized surface coil for RF transmission/reception was centered on the imaging slices covering the somatosensory cortex, and the brain was positioned close to the isocenter of the magnet. Magnetic field homogeneity was optimized by global shimming, followed by the FASTMAP shimming protocol on the ellipsoidal volume covering the cerebrum (ParaVision 6, Bruker BioSpin).

Calibration of the amount of contrast agent used for CBV-weighted fMRI studies. Gradient-echo (GE) echo planar imaging (EPI), commonly used in functional studies, is sensitive to susceptibility artifacts arising from implanted optic fibers, particularly at long TEs and high field strengths (Fig. S1A). Importantly, the BOLD contrast measured by GE-EPI is highly sensitive to draining veins, resulting in poor specificity for cortical layers. CBV-weighted fMRI with a superparamagnetic contrast agent is an alternative method to GE-BOLD to improve the functional sensitivity and spatial specificity for neuronal active sites (38). CBV-weighted fMRI with a short TE has the advantage of reducing nonspecific BOLD contributions and minimizing susceptibility artifacts. Initially, we measured the relationship between contrast doses and T_2^* by repeated injection of monocrystalline iron oxide nanoparticles (MIONs) into the tail vein until the cumulative dose reached 45 mg/kg (from 2 to 45 mg/kg) in 3 naïve mice (Fig. S1B). The T_2^*-weighted images were obtained using the multi-gradient-recalled echo (Multi-GRE) sequence with sixteen echo times = 1.5 to 18 ms and an interval of 1.1 ms,

repetition time (TR) = 0.8 s, field of view (FOV) = 15 (read-out, x-axis) × 7.5 (phase-encoding, y-axis) mm^2, matrix = 96 × 48, spatial resolution = 156 × 156 × 500 μm^3, flip angle = 50°, contiguous 6 coronal slices and number of excitations (NEX) = 4.

fMRI combined with optogenetics. Our imaging strategy was to use a very short TE for fMRI data without susceptibility artifacts while maximizing the functional sensitivity. Therefore, TE was set to 3 ms for matching to tissue T_2^* (3.44 ± 0.08 ms in Fig. S1B), with MION at a 45 mg/kg dose. CBV-weighted fMRI data were acquired after using the fast low-angle shot magnetic resonance imaging (FLASH) sequence with the following parameters: TR/TE = 50/3 ms, flip angle = 15°, FOV = 15 × 7.5 mm^2, matrix size = 96 × 48, partial Fourier = 1.2 along the phase-encoding direction, spatial resolution = 156 × 156 × 500 μm^3, 6 contiguous coronal slices and temporal resolution = 2 s. From individual transgenic mice (n = 22 mice), fMRI data were acquired under three stimulus conditions: optogenetic cortical silencing (n = 8 for S1FL targeting, n = 7 for M1, and n = 7 for S2), forepaw stimulation, and simultaneous silencing and forepaw stimulation. The three stimulus conditions were acquired in an interleaved manner, with an interscan interval longer than 3 mins. To address the potential heating-related artifacts induced by light, functional studies in naïve mice (n = 3) were interleaved between optogenetic and forepaw stimulations. For each stimulus condition, 15 fMRI trials were performed for each animal.

Resting-state fMRI. Conventional rs-fMRI, which is presumably related to the intrinsic network of spontaneous activity, was obtained to examine the resting-state somatosensory network. Ten 10-min rs-fMRI scans (i.e., 300 volumes) were obtained from a separate naïve animal group (n = 5, twice each) with the same imaging parameters used for fMRI with cortical inhibition, after a few somatosensory fMRI scans to ensure the physiological condition of the mice responding to external stimuli under anesthesia.

Data analysis

Electrophysiology data analysis. To detect the spiking activity, the extracellular recording traces were preprocessed as follows: first, raw data were high-pass filtered (> 300 Hz; 4th-order Butterworth filter); second, the common noise level was temporally removed by subtracting the trimmean (50%) filtered signals over all channels at each time point from each channel; third, MUA was quantified over 1 ms temporal bins by counting the number of spikes exceeding a threshold of 5 × median absolute deviation in 30 s of prestimulus baseline data (39). The LFP data were extracted from the extracellular recording traces by bandpass filtering at 1 to 280 Hz and downsampled to 1 kHz. For the comparison between trials with forepaw stimulation at 4 Hz and optogenetic silencing at 20 Hz, spike trains and LFP waveforms during stimulation were aligned with a 250-ms moving window after the first stimulus onset of each block, and repeated runs (20 s × 2 blocks × 4 windows/s × # of trials) were then averaged (Fig. S5B).

To confirm the suppression of spontaneous neural activities during optogenetic cortical stimulation, each light pulse-induced putative inhibitory neural activity was excluded for the 10 ms light pulse period and followed up for 10 ms, resulting in spontaneous spike activity during the 30 ms period following each 20 Hz stimulation pulse (40). The firing rates were calculated across the upper 8 and lower 8 channels to measure depth dependency.

To investigate the cortical depth-dependent MUA and LFP responses, we first performed inversion current source density (iCSD) analysis with the LFP waveform using the CSDplotter toolbox (41) to identify the location of L4. The synaptic inputs induced by forepaw stimulation were observed as a strong sink at depths of 0.4-0.56 mm, whereas the current sink generated by each optogenetic stimulation was shown at depths of 0.2-0.4 mm (Fig. S5C). Based on these laminar CSD profiles, the cortical depth of S1FL was assigned as L2/3, L4 and L5/6 (Fig. S5D and S5E).

We compared the spiking responses and field potential during optogenetic silencing without and with forepaw stimulation. Since somatosensory-evoked recurrent excitatory circuits are suppressed by

optogenetically activating inhibitory neurons in S1FL, remaining activity indicates direct feedforward inputs from the thalamus. The contribution of silenced local recurrent circuits is calculated by the difference between TC input-driven activity and the total somatosensory-evoked response. To alleviate minor response timing errors from the calculation, three sensory-evoked MUA traces and LFP waveforms (TC input-driven activity vs. local recurrent activity vs. total activity) were fitted using a single Gaussian function and double gamma-variate function, respectively, averaged across all channels and for each channel.

In the fitted MUA curve, activity parameters, including peak amplitude and AUC, and dynamic parameters, including onset time, peak time, and full width at half maximum (FWHM), were quantified. The response onset was defined as the first bin of five continuous bins whose spike rate differed significantly from the baseline activity ($p < 0.05$, one-sample t-test). In LFP, the same parameters described for MUA were calculated except for the onset time.

Calibration of the amount of contrast agent. To determine MION dose-dependent tissue T_2^*, multi-GRE data before and after every injection were fitted by a monoexponential function as $S_0 e^{-TE/T_2^*}$, where S_0 is the signal at TE = 0 ms. For quantification of tissue T_2^* changes, the ROI was defined as a 2D sphere with a radius of 500 μm centered on the anatomical location of S1FL with reference to the Allen mouse brain atlas.

Generation of fMRI maps. All MRI data were analyzed with the Analysis of Functional Neuroimages package (AFNI) (42), FMRIB Software Library (FSL) (43), Advanced Normalization Tools (ANTs) (44), and MATLAB codes (Mathworks, Nattick, USA).

To calculate group-averaged fMRI maps, a study-specific mouse brain template was constructed from CBV-weighted fMRI images based on a previously used pipeline (45, 46), as follows. First, the brain area was semiautomatically extracted from the temporal average of all fMRI images for each animal, and intensity nonuniformity was corrected with bias field estimation. Second, the individual fMRI

images were aligned with each other to select the most representative image requiring the least transformation within the population (43). Third, all the images were spatially normalized into that representative image using both linear and nonlinear transformation and averaged to generate the mouse brain template. To identify the anatomical location, the study-specific template was coregistered with the Allen mouse brain atlas (19).

The fMRI response maps for individual animals were generated using preprocessing and general linear model (GLM) analysis. The steps of preprocessing were previously described in detail (30, 45). In short, preprocessing included slice timing correction, image realignment for minor head motions, linear signal detrending for signal drift removal, and time course normalization by the average of the baseline period. All repeated fMRI trials per stimulus condition on each animal were averaged and spatially coregistered to study-specific brain templates. Then, spatial smoothing was applied with a Gaussian kernel of one-pixel FWHM to minimize the potential misalignment and to enhance the functional detectability. Individual fMRI maps were calculated by a GLM analysis based on the data-driven hemodynamic response function (HRF). The HRF was determined from the animal-wise averaged time course in S1FL during forepaw stimulation by fitting with a two-gamma variate function. After GLM analysis, group-averaged fMRI maps of forepaw stimulation (FP), optogenetic stimulation only (Opto), and combined forepaw and optogenetic stimulation (Comb) were generated for S1FL, M1 and S2 silencing condition with a one-sample t-test using nonparametric inference (43), with significance at threshold-free cluster enhancement (TFCE)-corrected $p < 0.05$. To determine the somatosensory input-driven response without the feedforward or local contribution from the inactivation site, fMRI time courses during optogenetic cortical inactivation with and without forepaw stimulation were subtracted (Comb – Opto), and difference maps (Diff) were obtained with a significance level of uncorrected $p < 0.01$ (paired t-test). In addition, all animal data ($n = 22$) were used for generating group-averaged FP activation maps. The group-averaged fMRI maps were overlaid on the study-specific brain template, and the fMRI active sites were determined according to the Allen mouse brain atlas.

For rs-fMRI data, preprocessing steps similar to those used for evoked fMRI were included: slice timing correction, image realignment, linear detrending, and voxel-wise time course normalization. To stabilize the functional connectivity, additional preprocessing steps were applied: spiking signal removal, data cleaning by regressing out nuisance variables including 12 motion confounds (6 parameters + temporal derivatives) and brain global signals, bandpass filtering ($0.01 < f < 0.2$ Hz) (35) and spatial smoothing with a Gaussian kernel of a 0.5 mm FWHM. Three seed ROIs of S1FL, M1, and S2 in the right hemisphere were anatomically defined based on the Allen mouse brain atlas. In common space, functional connectivity maps for individual animals were calculated by correlation analysis of the mean time courses of each seed ROI and voxel-wise time series in the whole brain. To generate group-averaged rs-fMRI maps, voxel-wise correlation coefficient (r) was converted to a normally distributed z-score using Fisher's r-to-z transformation, and a one-sample t-test was performed (TFCE-corrected $p < 0.05$). After statistical testing, the results were inversely transformed back to correlation coefficients to represent group-averaged rs-fMRI maps.

Quantitative region of interest analyses for circuit analysis. For quantitative analysis, five different ROIs corresponding to active sites during forepaw stimulation were defined based on the Allen mouse brain atlas: S1FL, M1, S2, VPL, and POm. Time courses from each ROI were obtained for FP, Opto, Comb, and Diff conditions in each animal, and fMRI signal changes were calculated by averaging responses over the stimulus condition, excluding the initial 6 s after stimulus onset to obtain steady-state positive or negative responses without the initial transition period. An increase in CBV increases the amount of iron oxides within the voxel, decreasing fMRI signals. Thus, the original CBV-weighted fMRI signal changes were inverted for better visualization in all analyses.

Resting-state fMRI analysis. Mean z-values within each ROI were calculated from rs-fMRI data, whereas percent signal changes induced by cortical silencing (S1FL, M1, and S2) were averaged. The degree of rs-fMRI coherence between two different regions often considers a proxy, resting-state neural network strength. To compare the relative strength of spontaneous functional connectivities measured

by rs-fMRI and cortical silencing fMRI, the magnitude of functional connectivity (z-scores) within predefined somatosensory ROIs was normalized to the strongest connectivity with a seed area in rs-fMRI (given a maximum z-value equal to 1), whereas the fMRI change in spontaneous connectivity during cortical silencing fMRI was normalized to the response at the optogenetic stimulation site.

Layer analysis of fMRI responses. To measure synaptic input layer-specific fMRI responses, cortical areas, including S1FL, M1, and S2, were flattened by radially projecting 22 lines perpendicular to the cortical edges (47). The cortical-depth profiles were resampled to double using bicubic interpolation. Group-averaged percent change maps were calculated from the percent change maps of individual animals. The fMRI signal changes within the same cortical depth were calculated in the same manner described above. Laminar boundaries for each cortex were defined as a cortical thickness distribution based on the Allen mouse brain atlas.

Statistics. All quantitative values are presented as the mean ± standard error of the mean (SEM). For comparison of suppression in spontaneous MUA firing rates with and without optogenetic inactivation (Fig. 1C), fMRI signal changes for measuring heating-related fMRI artifacts (Fig. 1E), fMRI signal changes between long-range sensory inputs (i.e., difference between cortical inactivation with and without forepaw stimulation) and total sensory-evoked activities (forepaw stimulation only) (Fig. 3C, 3D, 4C, 4D and 6B), and the relative fraction of long-range inputs and local recurrent activities in the MUA and LFP (Fig. 4G), a paired t-test was conducted to determine the statistical significance of differences. For comparison of fMRI signal changes across somatosensory fMRI experiments in different animal groups, one-way analysis of variance (ANOVA) was conducted (Fig. 3C, 3D, 4C, 4D and 6B). To compare the cortical depth-dependent MUA and LFP (Fig. S5F-H), one-way ANOVA with repeated measures was performed. All ANOVA tests were followed by the Bonferroni *post hoc* test for multiple comparisons. Statistical significance was considered at $p < 0.05$.

Results

To map brain-wide spontaneous and evoked long-range somatosensory networks with fMRI (Fig. 1A), VGAT-ChR2-EYFP mice expressing light-sensitive opsin proteins in GABAergic interneuron populations were used. An optical fiber cannula (105-μm inner core diameter) was implanted into S1FL, M1 or S2 to silence local pyramidal neuronal activities selectively and repeatedly via optogenetic stimulation of inhibitory neurons with blue light (473 nm, 3 mW, 10 ms duration, and 20 Hz) (Fig. 1B). The suppression of neural activities was confirmed by recording multiunit activities (MUAs) with 16-channel optoelectrodes under the same photostimulation conditions used for fMRI studies. During 20 s of photostimulation to S1FL, an increase in stimulation-induced inhibitory neuronal activity mostly suppressed spontaneous activities at all cortical depths (Fig. 1C; baseline (black bar) vs. light on (blue bar): 6.27 ± 1.54 Hz vs. 0.57 ± 0.19 Hz in the upper 8 channels; 18.82 ± 1.91 Hz vs. 2.27 ± 0.85 Hz in the lower 8 channels; $p < 0.01$; $n = 6$ mice), which is consistent with previous findings (33, 48).

Optogenetic fMRI of lightly anesthetized VGAT-ChR2 mice was performed with an ultrahigh magnetic field of 15.2 T. Fiber implantation often causes image distortions and signal dropouts in echo planar images commonly used for fMRI studies, which are more severe with higher magnetic fields (see red box of Fig. 1D; Fig. S1A). Thus, we adopted a conventional gradient-echo imaging technique with a short echo time (TE) of 3 ms to minimize draining vein-sensitive BOLD contributions and image distortions, which allows us to identify fiber position (see blue box of Fig. 1D; Fig. S1A) and coregister brain MRI with the mouse brain atlas. To enhance functional sensitivity and specificity, 45 mg/kg superparamagnetic iron oxide nanoparticles were injected into the blood (Fig. S1B for selection of the iron oxide dose), which resulted in CBV sensitization. An increase in CBV increases the amount of iron oxides within the voxel, decreasing fMRI signals. Thus, the polarity of the original CBV-weighted fMRI signal changes was inverted to match that of the CBV responses. Multislice CBV-weighted fMRI was obtained with spatial resolution = 156 × 156 × 500 μm^3 and temporal resolution = 2 s for mapping functional connectivity with highly specific blood volume responses. Photostimulation did not induce

heating-related fMRI artifacts in naïve mice (Fig. 1E; C57BL/6J, n = 3 mice); thus, fMRI responses to optogenetic stimulation genuinely reflect the underlying neural activity.

To dissect the functional circuits with fMRI, optogenetic cortical inhibition was adopted during somatosensory stimulation (Fig. 1F). Silencing cortical excitatory neurons by optogenetically activating ChR2-expressing inhibitory neurons suppresses outputs to downstream pathways (Opto in Fig. 1F), resulting in a decreased fMRI signal in downstream-networked areas (deactivation). This approach can be used to map spontaneous neural interactions at a resting state. Simultaneous forepaw stimulation during cortical silencing can preserve sensory-evoked inputs to the thalamus and cortex via upstream ST and TC pathways with downstream suppression (Comb in Fig. 1F). Since inhibitory neural activation induces a hemodynamic response (40, 49), its direct contribution can be removed by the difference between the optogenetic fMRI responses observed with and without sensory stimulation (Comb – Opto = Diff in Fig. 1F), and the remaining signal is due to the contribution of upstream ST and TC pathways in the absence of downstream projection from a given target region. Consequently, the contribution of downstream suppression to fMRI responses can be determined from somatosensory-evoked fMRI responses (Diff vs. FP in Fig. 1F), allowing us to determine functional causality for long-range and local processing in somatosensory networks. Although a similar circuit-analysis approach of sensory stimulation with and without local silencing has been used for electrophysiological studies in preselected areas (13-15), fMRI with and without optogenetic inhibition can determine brain-wide long-range circuits at a population level.

Mapping somatosensory networks of spontaneous activity: rs-fMRI vs. cortical silencing fMRI

First, we investigate the validity of commonly used rs-fMRI connectivity determined by synchronization of fluctuating fMRI signals between regions in the absence of a task, which is presumably related to the intrinsic network of spontaneous activity. Data from ten 10-min rs-fMRI scans (i.e., 300 volumes) were obtained from five naïve mice, and rs-fMRI connectivity to S1FL, M1, and S2

seed ROIs in the right hemisphere was mapped (Fig. 2A). Commonly observed strong bilateral homotopic cortical connectivity was detected without a significant network between the seed ROIs and the ipsilateral thalamus (Fig. 2A). This bilateral cortical connectivity may be due to direct CC communications and/or synchronized common neural and vascular sources. This issue was examined by focal cortical inhibition, which can suppress spontaneous CC communications.

Focal silencing of S1FL, M1, or S2 activity by optogenetic stimulation of inhibitory neurons reduces CBV in networked cortical and subcortical sites. Inactivation of S1FL induced negative CBV changes at the ipsilateral S1 (hindlimb, whisker barrel), M1, S2, thalamic nuclei including the ventral posterolateral nucleus (VPL) and POm, and striatum (see Fig. 2B for group-averaged fMRI maps; Fig. S3B for responses of individual animals; VGAT-ChR2, n = 8 mice), which are consistent with anatomical tracing studies (19). Similar observations were detected for inactivation of M1 (see Fig. 2B for group-averaged fMRI maps; Fig. S3C for responses of individual animals, n = 7 mice) and for the inhibition of S2 activity (Fig. 2B for group-averaged fMRI maps; Fig. S3D for responses of individual animals, n = 7 mice). Interestingly, S1FL and M1 have reciprocal connections with similar magnitudes, while the CT connection is stronger in POm than in VPL (Fig. 2B). To compare the networks measured by rs-fMRI and cortical silencing fMRI (Table. S1), the relative strength of spontaneous long-range functional connectivity was quantified by normalization with the strongest connectivity in rs-fMRI (Fig. 2D) and with the response at the stimulation site in cortical silencing fMRI (Fig. 2E). The commonly observed bilateral homotopic connections of rs-fMRI (50-56) were not clearly observed in networks during cortical inhibition, indicating that the bilateral cortical connectivity of rs-fMRI is unlikely to be due to direct neuron-based CC communication. Overall, brain-wide spontaneous networks can be mapped by fMRI with inhibition at focal sites.

Dissection of somatosensory activity-driven responses by cortical silencing

Somatosensory stimulation of the forepaw (0.5 mA, 0.5 ms duration, and 4 Hz) induced robust CBV

increases in the contralateral somatosensory network (see Fig. S2 for group-averaged fMRI maps; Fig. S3A for responses of individual animals, n = 22 mice). Brain-wide activation sites were observed in the cortex, including S1FL, M1, S2, and the thalamic nuclei, including the ventral posterolateral nucleus (VPL) and POm (Fig. S2B), suggesting that evoked responses to forepaw stimulation possibly contain ST, TC, CC and CT pathways. To dissect the functional circuits that evoked the fMRI response, optogenetic cortical inhibition was performed at S1FL, M1 and S2 in conjunction with forepaw stimulation.

Initially, we investigated the relative contribution of ST and CT circuits to thalamic fMRI responses (Fig. 3). To separate these two contributions to thalamic fMRI signals, fMRI responses to optogenetic silencing of the targeted cortex vs. simultaneous silencing and forepaw stimulation were compared. These differences are directly related to all inputs except the CT inputs from the target site to the thalamic nuclei ($Diff_{S1FL}$, $Diff_{M1}$, and $Diff_{S2}$ in Fig. 3A). In VPL, the CBV response to somatosensory stimulation was similar to the difference between cortical silencing and silencing/forepaw stimulation, regardless of S1FL, M1, or S2 silencing (Fig. 3B and 3C), suggesting that VPL is driven by inputs from the spinal cord, not from the cortex. In POm, S1FL silencing suppresses the fMRI response to forepaw stimulation completely, whereas M1 and S2 silencing has no impact (Fig. 3B and 3D), indicating that POm activity is directly driven by S1, not from ST inputs. This is consistent with previous electrophysiological studies (57, 58). With our fMRI approach, the relative contributions of feedback CT and feedforward ST activity to sensory-evoked thalamic responses were successfully determined.

Dissection of S1FL and M1 responses to TC, CC and IC activity

Next, we have examined the relative contribution of long-range inputs and local circuits to fMRI responses in S1FL and M1 (Fig. 4). The somatosensory-induced fMRI responses of S1FL can contain TC input from VPL, IC activity and CC feedback from M1 and S2, whereas the fMRI response of M1 can contain CC inputs and IC activity. The role of each pathway in somatosensory-evoked fMRI responses in S1FL and M1 was examined by optogenetic silencing of S1FL, M1, or S2 (Fig. 4A for

input circuit diagrams and Fig. 4B for corresponding fMRI maps).

We first examined the contributions of functional pathways to somatosensory-evoked M1 responses (Fig. 4C). The M1 response was completely suppressed when optogenetic S1FL silencing was performed (Diff (blue line) vs. FP (paired-black line) in Fig. 4C) but remained the same when S2 activity was silenced (Diff (red line) vs. FP (paired-black line) in Fig. 4C). This suggests that somatosensory-evoked M1 activity is mostly driven by the CC projection from S1FL. The CC input-driven magnitude response during M1 silencing accounts for approximately 36% of the total somatosensory-evoked fMRI response in M1 (Diff (green bar) vs. FP (paired-gray bar) in Fig. 4C). Since the input-driven CBV response duration (green line) is shorter than the total CBV response (paired-black line), the area under the curve (AUC) was also compared, revealing that the input-driven CBV response accounts for 24% of the total response. The somatosensory-evoked activity in M1 is driven by the S1FL feedforward projection and amplified via the IC circuitry.

Then, the contributions of the TC, IC and CC circuits were separated in the S1FL response (Fig. 4D). Based on fMRI data with M1 or S2 silencing, we found that the CC projection from M1 and S2 to S1FL is negligible during forepaw stimulation, indicating that there was no feedback CC long-range contribution to the sensory response in S1FL, as expected under anesthesia (59, 60). When S1FL activity was suppressed, the positive CBV response remained, with a reduced magnitude of approximately 31% of that of the total stimulus-driven response (Diff (blue line) vs. FP (paired-black line) in Fig. 4D) and 26% of that of the total AUC.

To investigate the neural source of the somatosensory-induced fMRI reduction caused by local silencing, 16-channel electrophysiological recordings were made in S1FL with the same stimulus paradigms as fMRI (Fig. 4E, VGAT-ChR2, n = 6 mice). Time-locked neural data for one forepaw stimulus pulse interval of 250 ms were obtained by averaging all 250-ms windows (FP). Inhibitory neuronal activities induced by optogenetic stimulation of GABAergic neurons were subtracted out by the difference between those responding to optogenetic stimulation with and without somatosensory stimulation (Diff). MUAs and local field potentials (LFPs) were compared across different experimental

conditions (see Fig. 4F and 4G for averaged responses across all 16 channels and Fig. S5 for depth-dependent responses). The difference between optogenetic silencing of S1FL and simultaneous silencing and forepaw stimulation (Diff) indicates neural activities induced by TC input, whereas somatosensory-driven activity contains both long-range input and local recurrent activity (Fig. 4F). Thus, the local recurrent activity (FP-Diff) can be obtained from the difference between long-range TC input (Diff) and total somatosensory activity induced by forepaw stimulation (FP; see inset figures in Fig. 4F). The thalamic input activity integrated over time was ~35% of the forepaw-induced neural activity (Fig. 4G; 37.73 ± 4.54% for MUA and 33.03 ± 5.92% for LFP; Table S2 for MUA and Table S3 for LFP), which is in good agreement with the fMRI observations (31% for magnitude, 26% for AUC). The somatosensory-evoked local recurrent activity suppressed by optogenetic silencing occurs ~6 ms later than the input activity (Fig. 4G; Diff vs. FP-Diff; 26.50 ± 1.43 ms vs. 32.83 ± 1.45 ms for MUA; 31.67 ± 1.52 ms vs. 38.00 ± 1.71 ms for LFP; Table S2 for MUA and Table S3 for LFP). Combined with macroscopic fMRI and microscopic electrophysiology data, these findings show that somatosensory-evoked TC activity is amplified by ~2-fold in S1FL due to local recurrent circuits (15), and fMRI can separate long-range input and local circuit contributions.

Then, we have examined whether TC and CC input layers in S1FL and M1 can be identified by cortical depth-dependent CBV responses (Fig. 5). Somatosensory-evoked CBV responses peaked at layer 4 (L4) of S1FL (Fig. 5B and 5C), indicating the TC input, and layer 2/3 (L2/3) of M1 (Fig. 5B and 5D), indicating the CC input. Cortical suppression in S1FL, M1 and S2 induced negative CBV changes in the optogenetic simulation site and peak responses in CC input layers of networked regions (Fig. 5B-D). When M1 is suppressed, the CC projection occurs at L2/3 and L5A, not L4 in S1 (61). Corresponding CBV peaks with different magnitudes were detected, with a small dip at ~150 μm-thick L4 (see Fig. 5C), indicating that the CBV response has a hemodynamic point spread function (PSF) of < 150 μm FWHM, which is somewhat similar to findings reported in olfactory bulbs (62). Our laminar-resolved fMRI data show that cortical CBV responses peak at synaptic input layers with high specificity.

Separation of the TC, CC, and CTC contributions to the sensory-evoked S2 response

Lastly, we have identified the relative contribution of long-range TC, CC and CTC inputs and local circuits to fMRI response in S2 (Fig. 6). The secondary somatosensory area is anatomically connected to VPL, POm, S1FL, and M1 (63). Thus, functional inputs to S2 during forepaw stimulation can originate from monosynaptic circuits from VPL (TC) and S1FL (CC) and disynaptic projections from S1FL via M1 (S1FL → M1 → S2) and POm (S1FL → POm → S2). When M1 activity was suppressed, the fMRI response at S2 remained the same (Diff (green bar) vs. FP (paired-gray bar) in Fig. 6B), indicating that the contribution of the S1 → M1 → S2 pathway is negligible. The contribution of the TC projection, calculated by the difference between the signal change without and with S1FL silencing, constitutes 25% of the total S2 response (Diff (blue bar) vs. FP (paired-gray bar) in Fig. 6B), whereas the remaining 75% of inputs originate from S1FL. When the sensory-evoked fMRI response was compared without and with S2 silencing, the CBV response of long-range synaptic inputs accounted for approximately 28% of the total percent change in S2 (Diff (red bar) vs. FP (paired-gray bar) in Fig. 6B; 30% of the total AUC), whereas the remaining response was due to local circuit contributions. These findings suggest that somatosensory-evoked S2 activity is mostly driven by feedforward S1FL inputs with minor VPL inputs and amplified by IC activity.

The synaptic inputs from S1FL to S2 can be direct S1FL (CC) inputs and/or indirect S1FL (CTC) inputs (64). Thus, our next question was whether the direct S1FL input to S2 (S1FL → S2) can be separated from the CTC input (S1FL → POm → S2). Since direct S1FL inputs project to layers 2/3 (L2/3) and L5 and CTC inputs project to L4 (Inputs to S2 in Fig. 6C) (61, 64, 65), cortical depth-dependent analysis may provide a clue concerning whether CTC inputs are dominant in the S2 fMRI response (Fig. 6C). Since laminar CBV responses are specific to synaptic input layers with a spatial PSF of < 150 μm (62), its peak position provides information on cortical input layers. During forepaw somatosensory stimulation, the laminar S2 response was broad around L2/3 and L4 (FP in Fig. 6C and black profile in Fig. 6D). To obtain somatosensory-evoked fMRI signals originating from VPL, the

difference in cortical responses between S1FL inactivation with and without forepaw stimulation was obtained ($Diff_{S1}$ in Fig. 6C and blue profile in Fig. 6D). Then, the S1FL input (FP-$Diff_{S1}$ in Fig. 6C and pink profile in Fig. 6D) to S2 was determined by subtracting the VPL input ($Diff_{S1}$) from the total sensory-evoked response (FP). The TC inputs peaked at L4 in medial S2 ($Diff_{S1}$ in Fig. 6C and blue profile in Fig. 6C), whereas the inputs from S1FL induced double peaks at L2/3 and L5 in ventral S2 (FP-$Diff_{S1}$ in Fig. 6C and pink profile in Fig. 6D), indicating direct CC projections. These TC and CC inputs to S2 are spatially segregated by approximately 0.47 mm in a dorsal-ventral direction ($Diff_{S1}$ (blue arrow) vs. FP-$Diff_{S1}$ (pink arrow) in Fig. 6C), which cannot be easily identified by microscopic tools with a small field of view. Based on our laminar-resolved CBV fMRI with cortical silencing, we successfully confirmed TC and direct CC inputs to S2.

Discussion

We developed fMRI approaches with highly specific CBV contrast and local optogenetic silencing to dissect spontaneous and functional brain-wide long-range networks and successfully determined the relative contribution of each somatosensory circuit to somatosensory-evoked fMRI responses in mice at the population level (Fig. 6E). The VPL response originates mostly from the spinal cord, whereas POm receives functional CT projections from S1FL. S1FL receives somatosensory input from VPL (see Fig. 5C) (64, 66), and M1 receives feedforward CC input from S1FL. S2 receives mostly direct CC input (~75%) from S1FL and a small amount of TC input (~ 25%). The long-range synaptic input in cortical areas is amplified approximately 2-fold by local IC circuits. Since our findings are consistent with electrophysiology studies at preselected sites (13-15, 22, 24, 57, 64), the fMRI approach to long-range circuit analysis is viable for mapping long-range functional circuits in the whole brain.

To identify the contribution of neural circuits to fMRI responses, complete inhibition of excitatory recurrent neuronal activity and downstream projection is assumed. In our MUA measurements across cortical layers in S1FL, optogenetic stimulation of inhibitory neurons reduced spontaneous MUA by ~90% (Fig. 1C), which is consistent with systematic electrophysiological studies in the literature (48), and suppressed somatosensory stimulation-induced IC recurrent circuits (Fig. 4F). The spatial extent of cortical inhibition is dependent on the laser power level and can be approximately 1 mm away from the laser center (48). In our fMRI studies, the somatosensory-evoked response in POm and M1 was completely suppressed when optogenetic stimulation of inhibitory neurons in the upstream S1FL was applied, suggesting that cortical inhibition is effective in blocking downstream projections.

Mapping spontaneous neural communication

Effective brain-wide spontaneous connectivity can be determined by fMRI with optogenetic silencing. Ipsilateral somatosensory-related regions responding to cortical inhibition overlapped with the active sites during somatosensory stimulation. Our finding is supported by recent multichannel recording

studies in multiple thalamic areas, in which the inactivation of spontaneous excitatory activities in dorsal cortical areas suppressed thalamic activity with a short latency (12). Spontaneous CT communication to the higher-order thalamic nucleus POm is stronger than that to the relay thalamic nucleus VPL, which is consistent with electrophysiological findings (12, 57). Similarly, wide-field calcium imaging studies of the primary somatosensory cortex also showed a decrease in calcium activity in the ipsilateral M1 during inactivation of spontaneous activity in S1 (67).

Spontaneous neural network strength can be measured by fMRI. In our studies, the spontaneous network strength in S1FL → M1 and S2 (-2.75% and -1.98% of the peak response in L2/3) was larger than the somatosensory-evoked response (1.74% and 1.39% of the peak response). The relatively high spontaneous activity is surprising but may be due to the use of ketamine for anesthesia. Ketamine is an N-methyl-D-aspartate (NMDA) receptor antagonist that inhibits interneurons at a low dose (68). Our anesthetic condition enhances spontaneous activities via cortical disinhibition (69), which will be reduced during wakefulness.

The important implications of mapping spontaneous neural communication are 1) identifying potential circuits to modulate behavior and 2) investigating the source of commonly used rs-fMRI correlations. First, optogenetic inhibition has been used to elucidate the involvement of brain regions and specific cell populations associated with behavior. However, the neural circuits involved in behaviors can be due to local or downstream circuits. Although anesthesia will change the strength of long-range connections, downstream circuits associated with behavior can be mapped by fMRI. Second, resting-state connectivity maps generated by focal cortical inhibition can explain neural sources of conventional rs-fMRI. In rodent rs-fMRI, a strong correlation occurs between bilateral homotopic cortices (50-56) but not between the cortex and thalamus in the ipsilateral hemisphere. This indicates that homotopic rs-fMRI coherence is unlikely to be due to direct bilateral CC neural communication. Thus, rs-fMRI coherence should not be interpreted as a direct neural interaction.

Long-range input vs. local circuit contributions to sensory-evoked fMRI

Somatosensory-evoked long-range circuits were successfully dissected by fMRI. The CC circuit of S1 and M1 has been extensively investigated anatomically and physiologically (61, 70-72). S1 and M1 are reciprocally connected; neural excitation in S1 rapidly propagates into neurons in L2/3 and L5A in M1, which reciprocally activate neurons in L2/3 and L5A in S1 via a feedback loop (71). In our studies (Fig. 5 for S1FL and M1 fMRI responses to forepaw stimulation and cortical inhibition), the feedforward projection from S1 to L2/3 in M1 was observed for evoked and spontaneous conditions, but the reciprocal feedback projection from M1 to L2/3 and L5 in S1 was observed only for spontaneous, not evoked, condition. Similarly, the sensory-evoked feedforward CC projection from S1 to L2/3 and L5 in S2 was observed without the reciprocal feedback projection. Although the S2 contributions to sensory-evoked responses in S1 and M1 are negligible in our studies, these projections may significantly contribute in other behavioral contexts, such as perception and decision-making (73-75). The difference between our study and physiological studies is likely due to anesthesia (59). To obtain functional brain-wide circuits relevant to behavior, it is essential to perform fMRI on behaving mice.

In our studies, the long-range inputs and IC circuit contributions to somatosensory-evoked fMRI responses were separated. The long-range synaptic input-driven fMRI response in S1FL, S2, and M1 accounts for ~30% of the total somatosensory-evoked response. Similarly, somatosensory-evoked MUA and LFP in S1FL were reduced to ~35% of the total evoked neural activity by S1FL silencing. Therefore, the suppressed response, ~70% of the total fMRI response (~65% for MUA and LFP), is related to local neural activity. Our finding of a > 2-fold increase in the IC fMRI signal is somewhat consistent with electrophysiology data showing an approximately 2.2-fold amplification of IC in the barrel cortex (13), a 2.4-fold amplification of IC in the primary auditory cortex (14) and a 3-fold amplification of IC in the primary visual cortex (15), in which TC and IC activities were separated with recordings of excitatory cells in L4 after optogenetic excitation of inhibitory neurons. Overall, fMRI with and without cortical inhibition can be used to identify the contributions of long-range input vs. IC circuits, facilitating the detection of cortical excitatory/inhibitory imbalance and consequent dysfunction of IC recurrent circuits.

We investigated POm and VPL in the thalamus. Consistent with previous studies (57), somatosensory-evoked responses in POm were drastically reduced after S1 inhibition, while VPM responses were not modulated. According to our data, the medial thalamic area adjacent to POm was active during somatosensory stimulation and S1FL silencing. This observation may be due to the spillover of POm activity with limited spatial resolution and group averaging and/or due to real activation in intralaminar nuclei, which are associated with multimodal sensory activity (76). Thus, fMRI experiments with higher spatial resolution are needed to determine whether the medial thalamic activity is genuine.

Overall, the fMRI approach with cortical silencing can be extended for investigations of brain-wide functional circuits induced by external stimuli or direct cortical stimulation. Evoked stimulation can be achieved via external or IC approaches with optogenetic or electric stimulation, activating entire networks without knowledge of the exact flow direction except for the target site. Thus, localized silencing is necessary to suppress downstream networks, which can be achieved by optogenetic stimulation with high temporal specificity, and pharmacological and photochemical tools for bulk interventions for specific neurotransmitter inputs to a defined brain region with low temporal specificity (10). The advantage of optogenetic tools is the ability to perform fMRI experiments under external stimulation with and without cortical silencing in an interleaved manner, which is essential for signal averaging without bias by slowly modulating animal physiology during imaging studies.

Conclusion

Here, we successfully dissected the brain-wide somatosensory circuits underlying fMRI responses. Our fMRI approach combining stimulation and focal inhibition opens a new avenue for understanding population-based neural circuits throughout the whole brain, allowing longitudinal investigations of functional reorganization caused by neuropathological modifications and learning in individual animals. Circuit-level analysis of whole-brain fMRI will complement conventional microscopic functional circuit studies by providing brain-wide, population-based information processing.

Acknowledgments

This project was funded by the Institute for Basic Science in Korea (IBS-R015-D1). We thank Prof. Joonyeol Lee and Kamil Uludag for critically reviewing this manuscript, Mr. Andrew You for helpful discussions, and Geun Ho Im and Chanhee Lee for maintaining the magnetic resonance imaging (MRI) instruments.

Figure legends

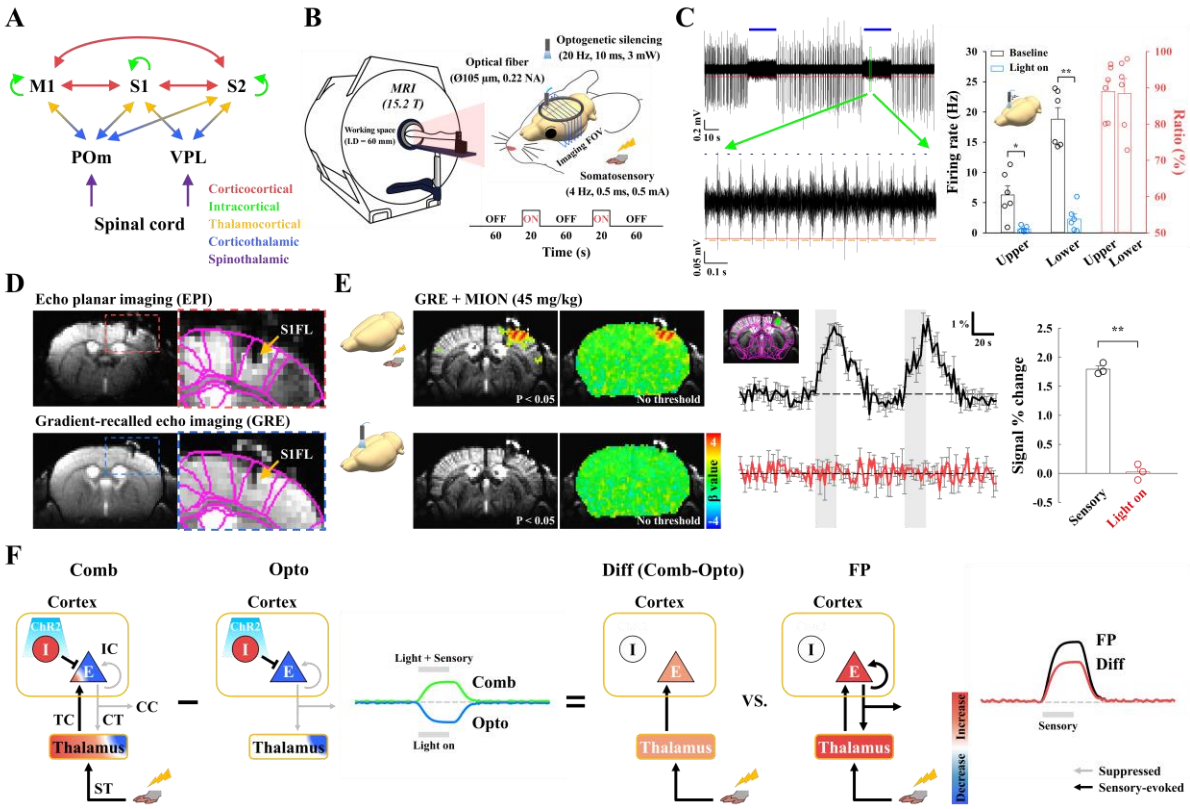

Figure 1. Experimental setup for high-resolution CBV-weighted optogenetic mouse fMRI and conceptual neural circuit analysis.

(A) Possible somatosensory network with local- and long-range reciprocal connections. The somatosensory inputs carried from the spinothalamic pathway are relayed to cortical areas via the thalamic nuclei. The cortex has long-range reciprocal loops with the thalamic nuclei and other cortical areas as well as local circuits to process sensory signals.

Corticocortical pathway, red; intracortical pathway, green; thalamocortical pathway, yellow; corticothalamic pathway, blue; spinothalamic pathway, purple.

(B) Schematic of multislice fMRI at 15.2 T during cortical inactivation with and without forepaw somatosensory stimulation.

(C) Silencing spontaneous activity of excitatory neurons in S1FL by optogenetic excitation of inhibitory neurons in VGAT-ChR2 mice (n=6). In recordings of MUAs with 16-channel optoelectrodes during 20 s of photostimulation, spontaneous activities in both the upper and lower 8 channels were mostly suppressed by activation of inhibitory neurons.

Blue horizontal bar, 20-s optogenetic stimulus; red, MUA amplitude threshold; yellow, spontaneous MUA count duration; error bar, SEM; *$p < 0.05$ and **$p < 0.01$ (paired t-test).

(D) High-resolution MRI images of the brain with an optical fiber targeting S1FL. The image artifacts of distortion and signal drop caused by the optical fiber in gradient-echo EPI (red-dashed box) were minimized by adoption of gradient-echo imaging with a short echo time of 3 ms (yellow arrow, fiber position). For the CBV-weighted fMRI study, a 45 mg/kg dose of a superparamagnetic monocrystalline iron oxide nanoparticle (MION) agent was injected into the blood. S1FL, primary somatosensory area of forelimb

(E) No artifactual fMRI response to light stimulation in naïve mice. To assess potential light-induced MRI artifacts, functional studies in naïve mice were conducted with interleaved forepaw stimulation and photostimulation of S1FL with the same experimental protocol used for fMRI with cortical inactivation (n=3). Somatosensory fMRI was used as the internal control to ensure the reliability of fMRI responses to external stimuli. Sensory-evoked fMRI responses were observed in S1FL, but responses during photostimulation were absent in fMRI maps with and without a statistical threshold (uncorrected $p < 0.05$) and in time courses of S1FL. Thus, fMRI signal changes resulting from light-induced tissue heating were negligible.

Gray vertical bar in time courses, 20-s stimulus; error bars, SEM; **$p < 0.01$ (paired t-test).

(F) Schematic diagrams to dissect sensory-evoked long-range and local activities by fMRI with the assistance of optogenetic cortical inhibition. Silencing cortical excitatory neurons by activating ChR2-expressing cortical inhibitory neurons suppresses outputs to downstream CT, CC and IC pathways (Opto), while simultaneous forepaw stimulation induces sensory-evoked upstream ST and TC inputs to the thalamus and cortex, respectively (Comb). After subtracting fMRI responses to optogenetic inactivation without forepaw stimulation from those with forepaw stimulation, difference signal is related to upstream input-driven responses (Diff) without the direct contribution of inhibitory neural activity. The relative contribution of downstream CT, CC and IC pathways can be determined from the total sensory-evoked activity (Diff vs. FP).

E, excitatory cell; I, inhibitory cell; ST, spinothalamic pathway; TC, thalamocortical pathway; CT, corticothalamic pathway; CC, corticocortical pathway; IC, intracortical pathway; blue-to-red color scale, decrease-to-increase relative to baseline activity.

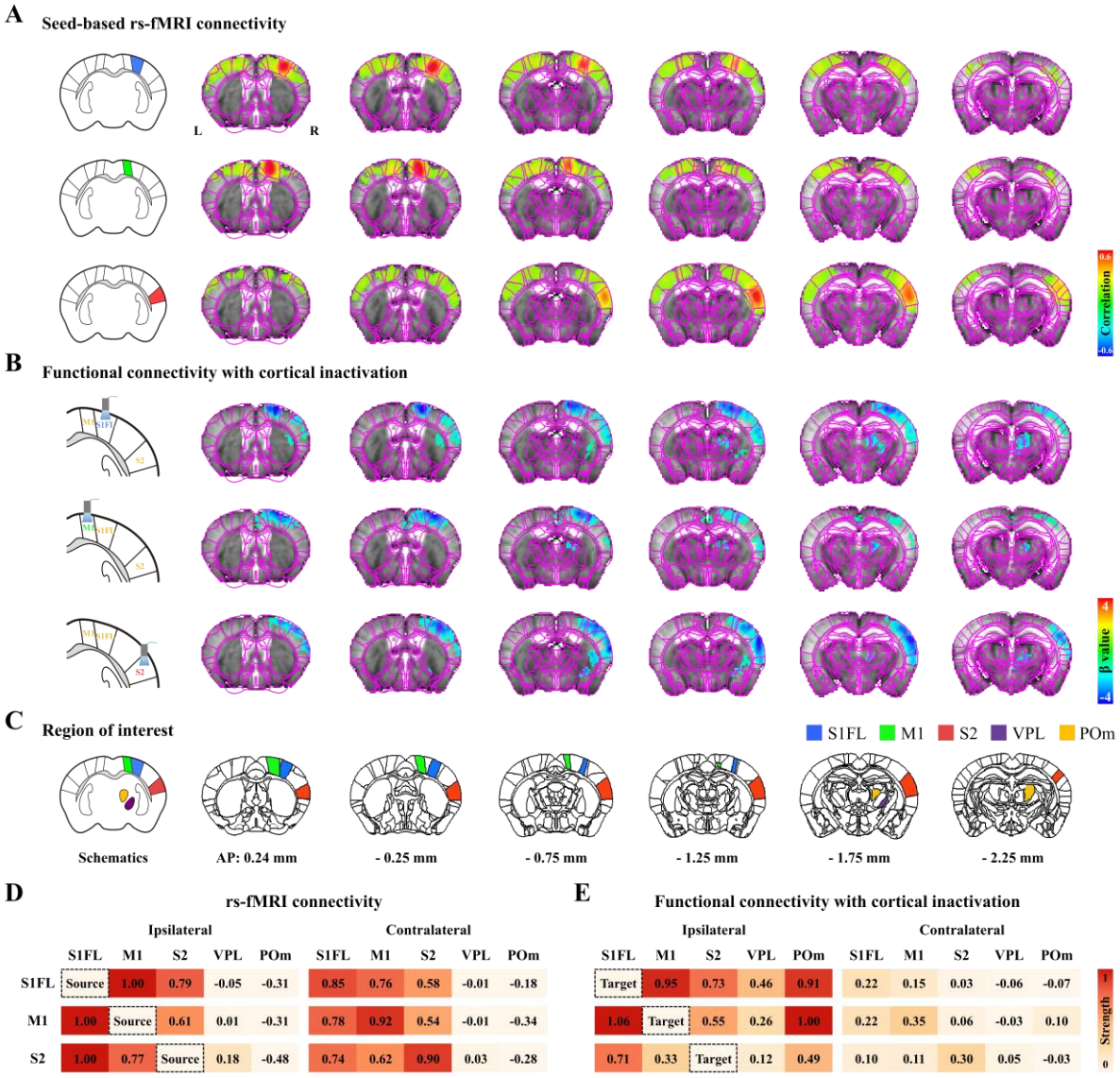

Figure 2. The spontaneous resting-state somatosensory network with optogenetic neuronal inactivation differs from conventional resting-state fMRI connectivity.

(A-B) Brain-wide functional connectivity maps of spontaneous activities measured by seed-based rs-fMRI and fMRI with cortical inactivation. Brain atlas drawings (in the most left) show seed ROIs and optogenetic stimulation site. **(A)** Strong bilateral homotopic correlations were observed in seed-based rs-fMRI for S1FL (wild-type, n=5), M1 and S2, whereas **(B)** ipsilateral somatosensory regions, including the cortices and thalamic nuclei, responded to optogenetic cortical inactivation of S1FL with a CBV decrease (VGAT-ChR2, n=8), M1 (n=7) and S2 (n=7).

(C) Allen mouse brain atlas-based anatomic ROIs in the somatosensory network. S1FL, primary somatosensory area of forelimb; M1, primary motor area; S2, secondary somatosensory area; VPL, ventral posterolateral nucleus;

POm, posterior medial nucleus.

(D-E) Functional connectivity matrices of the somatosensory network measured by rs-fMRI vs. fMRI with cortical inactivation. For the relative strength of functional connectivity, **(D)** degrees of resting-state connectivity were normalized to the strongest connectivity with source areas, while **(E)** fMRI signal changes in somatosensory-related ROIs in each hemisphere were normalized to those in the optogenetic target region. These two resting-state connectivity strength indices are not similar, indicating that the bilateral homotopic connectivity of rs-fMRI is unlikely to be due to direct corticocortical neural communication.

Red-to-orange color scale, relative strength of connectivity with source or target areas.

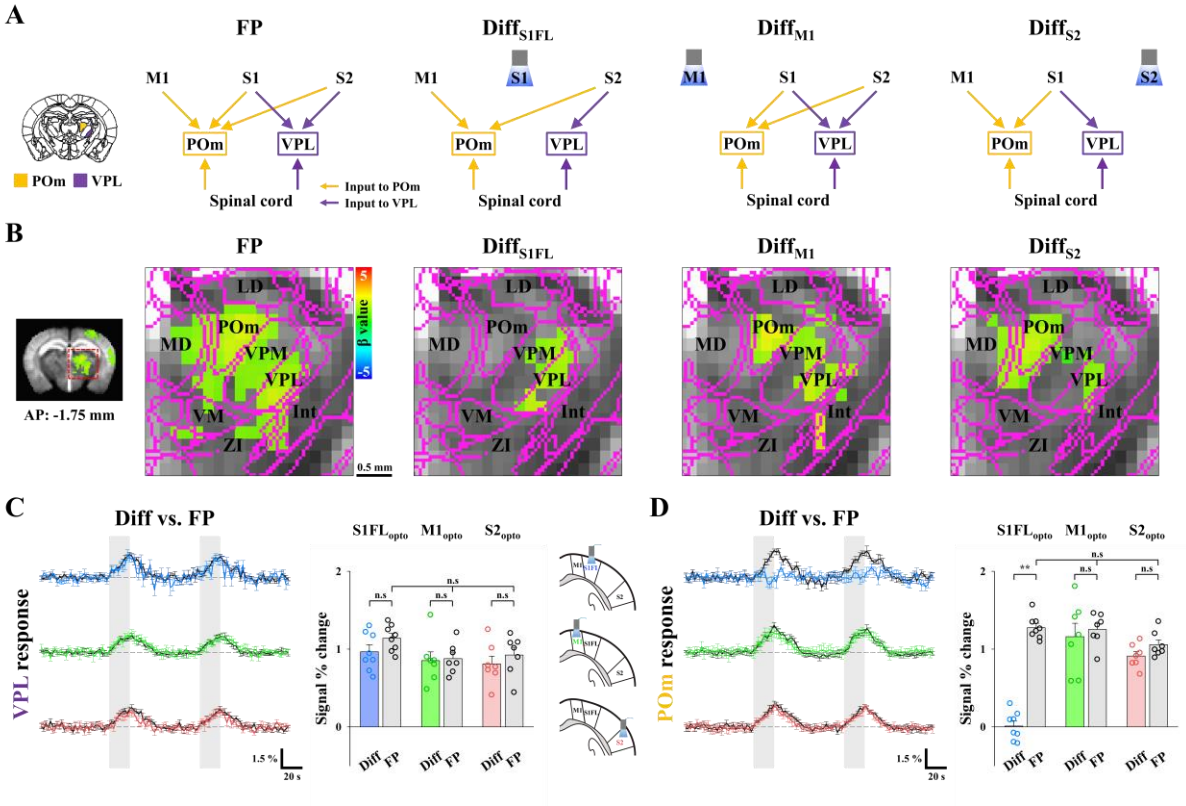

Figure 3. Dissection of somatosensory-driven thalamic fMRI responses with cortical silencing.

(A) Schematic diagrams to determine the contribution of long-range inputs to somatosensory-evoked thalamic fMRI responses with the optogenetic cortical inhibition. Functional activities in thalamic nuclei during forepaw stimulation (FP) can originated from multiple long-range inputs via ST and CT pathways, whereas difference in thalamic fMRI responses (Diff with a subscript indicating the inactivation site) between optogenetic cortical inactivation with and without sensory stimulation are related to all possible inputs except those from the target cortex of S1FL, M1 and S2 to the thalamic nuclei; thus, with comparison of those conditions (Diff vs. FP), the contribution of each pathway to thalamic response was investigated. VPL, ventral posterolateral nucleus; POm, posterior medial nucleus.

(B) fMRI maps in the thalamic nuclei. Forepaw (FP) stimulation induced activity in two distinct foci, VPL and POm (FP: n=22). Somatosensory-evoked activities in VPL were maintained in the fMRI difference maps (Diff) between optogenetic cortical inactivation with and without forepaw stimulation, whereas POm activity disappeared in the difference map of S1FL inactivation (Diff$_{S1FL}$: n=8) but not M1 (Diff$_{M1}$) and S2 (Diff$_{S2}$) inactivation (n=7, each). LD, lateral dorsal nucleus; MD, mediodorsal nucleus; POm, posterior medial nucleus; VPM, ventral posteromedial nucleus; VPL, ventral posterolateral nucleus; VM, ventral medial nucleus; Int, internal capsule; ZI, zona incerta; scale bar, 0.5 mm.

(C-D) Contribution of functional pathways to somatosensory-evoked VPL and POm responses. fMRI time courses in **(C)** VPL and **(D)** POm for the difference between combined stimulation and cortical silencing (Diff, colored

lines) and those for forepaw stimulation only (FP, black lines) were compared. **(C)** Under cortical silencing with and without forepaw stimulation, those differential responses (colored bar) are similar to the total VPL responses (paired-gray bar), **(D)** whereas the sensory-evoked POm response was completely suppressed during S1FL silencing (blue bar) but not during M1 (green bar) and S2 (red bar) silencing. Therefore, VPL has dominant inputs from the spinal cord, not the cortex, and POm activity is directly driven by S1FL, not from the spinal cord.

Gray vertical bar in time courses, 20-s stimulus; error bars, SEM; $^{**}p < 0.01$ (paired t-test).

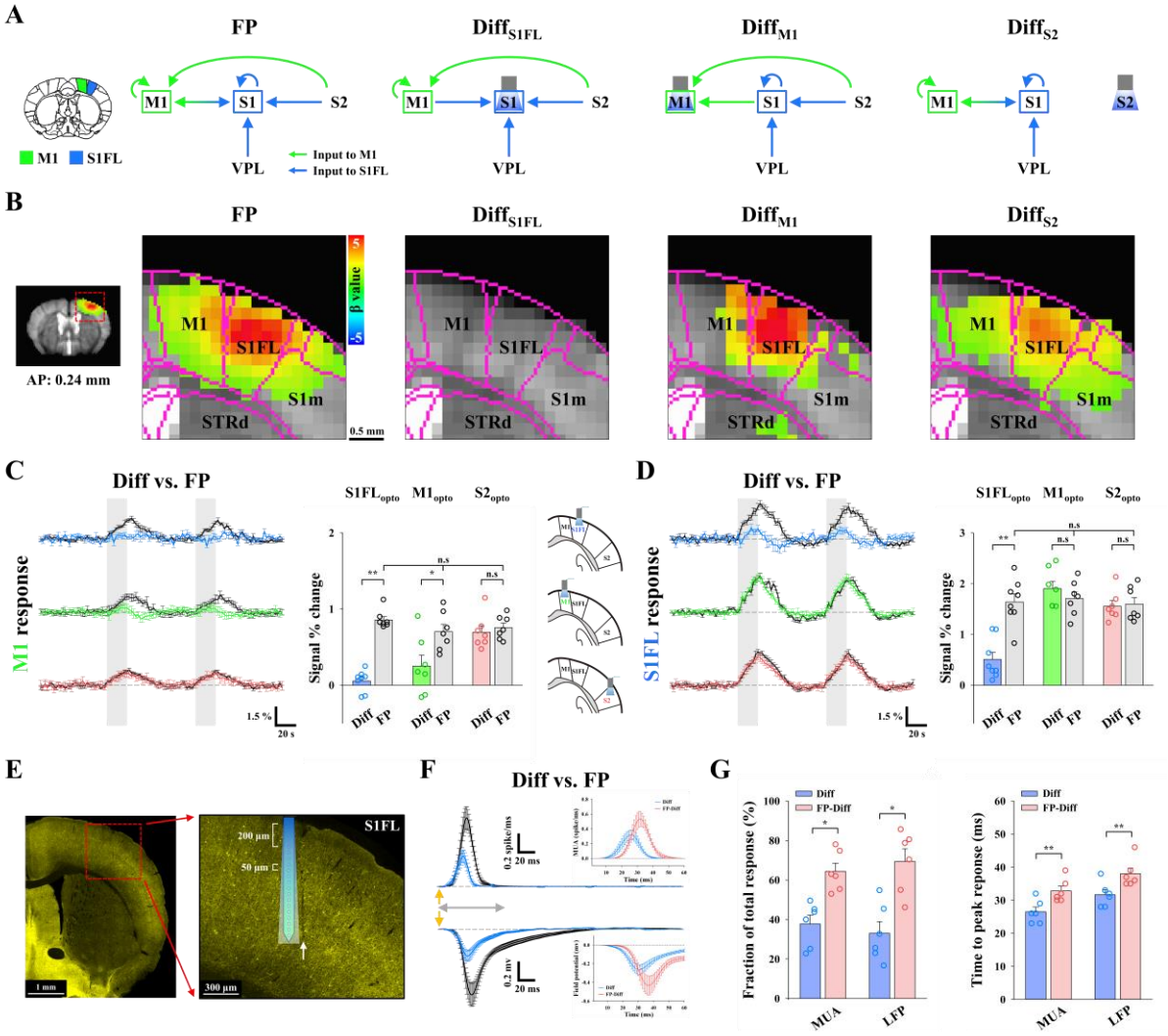

Figure 4. Dissection of TC, CC and IC activities during somatosensory fMRI responses in S1FL and M1.

(A) Schematic diagrams to determine the contribution of long-range and local activities to somatosensory-evoked M1 and S1FL responses with the optogenetic cortical inhibition. Functional activity in S1FL during forepaw stimulation (FP) can originated from both long-range inputs via TC and CC pathways and local IC activities, whereas M1 response can contain CC inputs and IC activity. The differences in cortical responses between optogenetic cortical inactivation with and without sensory stimulation (Diff) are related to input-driven activities, excluding CC and/or IC activities from the inactivation site (indicated as a subscript). M1, primary motor area; S1FL, primary somatosensory area of forelimb.

(B) fMRI maps in cortical areas including M1 and S1FL. Somatosensory-evoked activities in M1 (FP: n=22) disappeared in the fMRI difference map between M1 (Diff$_{M1}$: n=7) or S1FL (Diff$_{S1FL}$: n=8) optogenetic inactivation with and without forepaw stimulation but remained after S2 inactivation (Diff$_{S2}$: n=7), whereas

somatosensory-evoked S1FL responses disappeared only after S1FL inactivation. M1, primary motor area; S1FL, primary somatosensory area of forelimb; S1m, primary somatosensory area of mouth; STRd, striatum of dorsal region.

(C-D) Contribution of functional pathways to somatosensory-evoked M1 and S1FL responses. fMRI time courses in **(C)** M1 and **(D)** S1FL to determine the difference between combined stimulation and cortical silencing (Diff, colored lines) and those for forepaw stimulation only (FP, black lines) were compared. **(C)** The differential response in M1 (green bar) between M1 silencing with and without forepaw stimulation was approximately one-third of the total M1 response (paired-gray bar), and the sensory-evoked M1 response was mostly suppressed after S1FL silencing (blue bar) but not after S2 silencing (red bar). **(D)** The difference in S1FL response between S1FL silencing with and without forepaw stimulation (blue bar) is related to TC input, which accounts for approximately one-third of the total S1FL response (paired-gray bar). However, sensory-evoked S1FL responses were not changed by M1 (green bar) and S2 (red bar) silencing. Therefore, the M1 fMRI response is dominantly driven by S1FL, and the S1FL fMRI response is directly driven by VPL, with minimal corticocortical contribution; both of these responses are amplified by intracortical circuits.

Gray vertical bar in time courses, 20-s stimulus; error bars, SEM; *$p < 0.05$ and **$p < 0.01$ (paired t-test).

(E-G) Electrophysiological recording with the 16-channel opto-electrode to investigate the neural source of the S1FL fMRI response. **(E)** Fluorescence microscopy image from a representative animal shows the expression of ChR2-EYFP (yellow) in S1FL and the location of the electrode track (white arrow). **(F)** Neural data were time-lock averaged for the forepaw stimulus interval of 250 ms. Depth-averaged neural responses (MUA and LFP, VGAT-ChR2, n=6) in S1FL for the difference between combined stimulation and S1FL silencing (Diff, blue lines) and those for forepaw stimulation only (FP, black lines) were compared to isolate the local IC activity (FP-Diff, red lines in inset). Detailed depth-dependent responses can be found in Figure. S4. **(G)** Fraction and time to peak of sensory inputs (blue bar) and IC activity (red bar) in MUA and LFP.

Yellow arrows in **(F)**, 0.5-ms forepaw stimulus; gray double arrows in **(F)**, 60-ms period for the inset figure; error bars, SEM; *$p < 0.05$ and **$p < 0.01$ (paired t-test).

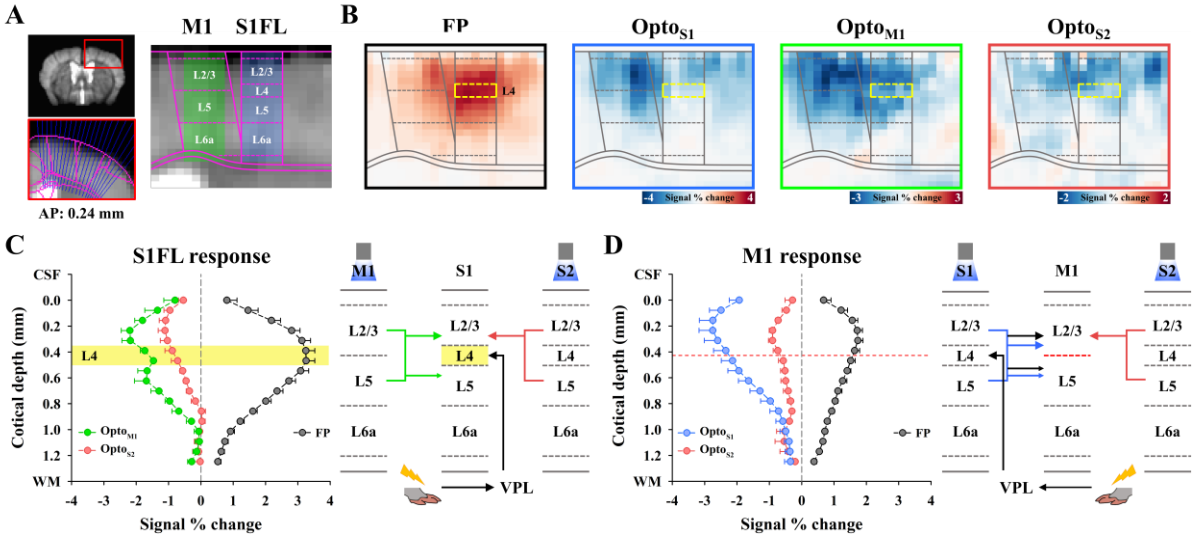

Figure 5. The highest CBV responses at synaptic input layers in S1FL and M1.

(A) Cortical flattening for layer-specific fMRI analysis in S1FL and M1. The cortical area (red box) was linearized using radially projecting lines perpendicular to the cortical edges (underlay, study-specific brain template; overlay, Allen mouse brain atlas). Laminar boundaries for each cortex were defined as the laminar thickness distribution.

(B) Cortical depth-dependent fMRI maps for somatosensory-evoked and spontaneous activities. Somatosensory-evoked activities (FP: n=22) were localized at L4 of S1FL (yellow-dashed box) and L2/3 of M1. Strong suppression occurred at L2/3 of S1FL and M1 during optogenetic cortical inactivation (Opto$_{S1}$: n=8, Opto$_{M1}$: n=7, Opto$_{S2}$: n=8).

(C-D) Cortical depth-dependent CBV profiles and expected circuit diagrams. Signal changes were averaged for the same depth and plotted as a function of distance from the surface in **(C)** S1FL and **(D)** M1. **(C)** The somatosensory-evoked response (black) peaked at L4 of S1FL, while M1 inactivation (green) induced two cortical peaks at L2/3 and L5, and S2 silencing (red) induced the largest changes at L2/3. Since ~150-µm-thick L4 of S1FL does not receive inputs from M1, the cortical profile responding to M1 stimulation indicates that the PSF of laminar CBV response is less than 150 µm FWHM. **(D)** The largest fMRI changes in M1 were mostly detected at L2/3, regardless of the type of stimulus.

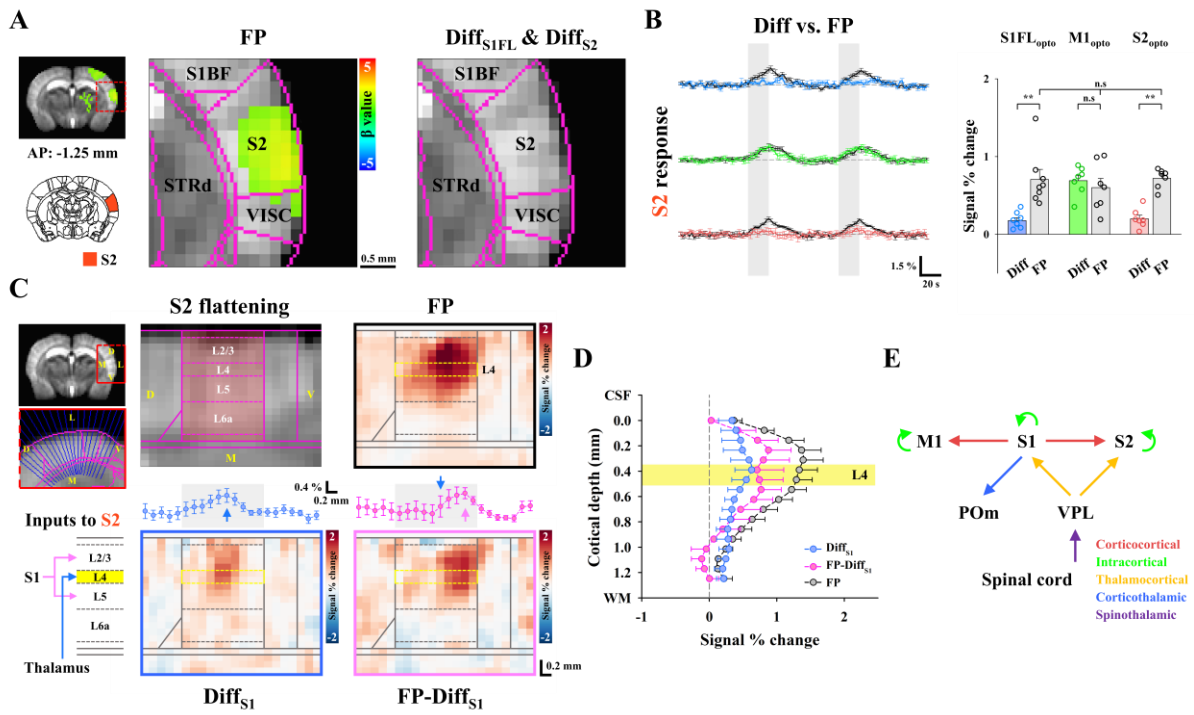

Figure 6. Separation of TC, CC, and CTC contributions to sensory-evoked fMRI responses in S2.

(A) fMRI maps in cortical areas including S2. Somatosensory-evoked activities in S2 (FP: n=22) disappeared in the fMRI difference map between S1FL or S2 optogenetic inactivation with and without forepaw stimulation (Diff$_{S1FL}$: n=8, Diff$_{S2}$: n=7) but remained after M1 inactivation (not shown here). S1BF, primary somatosensory area of barrel field; S2, secondary somatosensory area; VISC, visceral area; STRd, striatum of dorsal region.

(B) Contribution of functional pathways to the somatosensory-evoked S2 response. fMRI time courses in S2 for the difference between combined stimulation and cortical silencing (Diff, colored lines) and those obtained for forepaw stimulation only (FP, black lines) were compared. Under S2 silencing with and without forepaw stimulation, the difference response in S2 (red bar) was approximately one-third of the total S2 response (paired-gray bar). The sensory-evoked S2 response was largely suppressed in S1FL silencing (blue bar) but still had TC input (~25% of the total S2 response) and was not changed by M1 silencing (green bar). Therefore, the S2 fMRI response is predominantly driven by S1FL with a minor VPL contribution and amplified by intracortical circuits.

Gray vertical bar in time courses, 20-s stimulus; error bars, SEM; **$p < 0.01$ (paired t-test).

(C) Layer-specific fMRI analysis in S2. Thalamic inputs including both TC and CTC circuits project to L4, whereas direct S1FL inputs project to L2/3 and L5 (Inputs to S2). The S2 area was linearized using radially projecting lines perpendicular to the cortical edges (underlay, study-specific brain template; overlay, Allen mouse brain atlas). Laminar boundaries were defined as cortical thickness distribution (S2 flattening). To separate layer-specific TC inputs and direct/indirect S1FL inputs to S2 from the total sensory-evoked response, fMRI responses for the difference between combined stimulation and S1FL silencing (Diff$_{S1}$, TC inputs) and those for forepaw

stimulation only (FP from dataset paired with $Opto_{S1}$) were compared (FP-$Diff_{S1}$, direct/indirect S1FL inputs). In S2 flattened maps, somatosensory evoked responses were averaged across the cortical layers, and plotted in a dorsal-to-ventral direction (left-to-right). The patches responding to TC (blue line in $Diff_{S1}$) and direct/indirect S1FL (pink line in FP-$Diff_{S1}$) inputs were separable.

Blue ($Diff_{S1}$) and pink (FP-$Diff_{S1}$) arrows; locations of the response peak.

(D) For the cortical depth-dependent profile, signal changes were averaged for the same depth and plotted as a function of distance from the surface in S2. During the sensory-evoked response in S2 (FP, black line), the laminar profile for TC inputs peaked at L4 of S2 ($Diff_{S1}$, blue line), while the cortical profile projected from S1FL was observed to have double-peak responses at L2/3 and L5 (FP-$Diff_{S1}$, pink line), indicating direct CC inputs.

(E) Putative functional pathways in the somatosensory network as measured by CBV-weighted fMRI with optogenetic cortical silencing.

References

1. S. Ogawa *et al.*, Intrinsic signal changes accompanying sensory stimulation: functional brain mapping with magnetic resonance imaging. *Proceedings of the National Academy of Sciences of the United States of America* **89**, 5951-5955 (1992).
2. K. K. Kwong *et al.*, Dynamic magnetic resonance imaging of human brain activity during primary sensory stimulation. *Proceedings of the National Academy of Sciences of the United States of America* **89**, 5675-5679 (1992).
3. P. A. Bandettini, E. C. Wong, R. S. Hinks, R. S. Tikofsky, J. S. Hyde, Time course EPI of human brain function during task activation. *Magnetic resonance in medicine* **25**, 390-397 (1992).
4. B. Biswal, F. Z. Yetkin, V. M. Haughton, J. S. Hyde, Functional connectivity in the motor cortex of resting human brain using echo-planar MRI. *Magnetic resonance in medicine* **34**, 537-541 (1995).
5. M. D. Greicius, B. Krasnow, A. L. Reiss, V. Menon, Functional connectivity in the resting brain: a network analysis of the default mode hypothesis. *Proceedings of the National Academy of Sciences of the United States of America* **100**, 253-258 (2003).
6. M. D. Fox, M. E. Raichle, Spontaneous fluctuations in brain activity observed with functional magnetic resonance imaging. *Nature reviews. Neuroscience* **8**, 700-711 (2007).
7. M. P. van den Heuvel, H. E. Hulshoff Pol, Exploring the brain network: a review on resting-state fMRI functional connectivity. *European neuropsychopharmacology : the journal of the European College of Neuropsychopharmacology* **20**, 519-534 (2010).
8. N. K. Logothetis, What we can do and what we cannot do with fMRI. *Nature* **453**, 869-878 (2008).
9. K. Deisseroth, Optogenetics: 10 years of microbial opsins in neuroscience. *Nature neuroscience* **18**, 1213-1225 (2015).
10. J. S. Wiegert, M. Mahn, M. Prigge, Y. Printz, O. Yizhar, Silencing Neurons: Tools, Applications, and Experimental Constraints. *Neuron* **95**, 504-529 (2017).
11. K. Reinhold, A. D. Lien, M. Scanziani, Distinct recurrent versus afferent dynamics in cortical visual processing. *Nature neuroscience* **18**, 1789-1797 (2015).
12. Y. Huo, H. Chen, Z. V. Guo, Mapping Functional Connectivity from the Dorsal Cortex to the Thalamus. *Neuron* **107**, 1080-1094.e1085 (2020).
13. K. Cohen-Kashi Malina, B. Mohar, A. N. Rappaport, I. Lampl, Local and thalamic origins of correlated ongoing and sensory-evoked cortical activities. *Nature communications* **7**, 12740 (2016).
14. L. Y. Li, Y. T. Li, M. Zhou, H. W. Tao, L. I. Zhang, Intracortical multiplication of thalamocortical signals in mouse auditory cortex. *Nature neuroscience* **16**, 1179-1181 (2013).
15. A. D. Lien, M. Scanziani, Tuned thalamic excitation is amplified by visual cortical circuits.

Nature neuroscience **16**, 1315-1323 (2013).

16. Y. T. Li, L. A. Ibrahim, B. H. Liu, L. I. Zhang, H. W. Tao, Linear transformation of thalamocortical input by intracortical excitation. *Nature neuroscience* **16**, 1324-1330 (2013).
17. J. F. Staiger, C. C. H. Petersen, Neuronal Circuits in Barrel Cortex for Whisker Sensory Perception. *Physiological reviews* **101**, 353-415 (2021).
18. D. Feldmeyer *et al.*, Barrel cortex function. *Progress in neurobiology* **103**, 3-27 (2013).
19. S. W. Oh *et al.*, A mesoscale connectome of the mouse brain. *Nature* **508**, 207-214 (2014).
20. L. W. Bosman *et al.*, Anatomical pathways involved in generating and sensing rhythmic whisker movements. *Frontiers in integrative neuroscience* **5**, 53 (2011).
21. J. A. Harris *et al.*, Hierarchical organization of cortical and thalamic connectivity. *Nature* **575**, 195-202 (2019).
22. M. E. Diamond, M. Armstrong-James, M. J. Budway, F. F. Ebner, Somatic sensory responses in the rostral sector of the posterior group (POm) and in the ventral posterior medial nucleus (VPM) of the rat thalamus: dependence on the barrel field cortex. *The Journal of comparative neurology* **319**, 66-84 (1992).
23. S. Lee, I. Kruglikov, Z. J. Huang, G. Fishell, B. Rudy, A disinhibitory circuit mediates motor integration in the somatosensory cortex. *Nature neuroscience* **16**, 1662-1670 (2013).
24. I. Petrof, A. N. Viaene, S. M. Sherman, Properties of the primary somatosensory cortex projection to the primary motor cortex in the mouse. *Journal of neurophysiology* **113**, 2400-2407 (2015).
25. A. Agmon, B. W. Connors, Thalamocortical responses of mouse somatosensory (barrel) cortex in vitro. *Neuroscience* **41**, 365-379 (1991).
26. D. J. Simons, G. E. Carvell, Thalamocortical response transformation in the rat vibrissa/barrel system. *Journal of neurophysiology* **61**, 311-330 (1989).
27. I. Ferezou *et al.*, Spatiotemporal dynamics of cortical sensorimotor integration in behaving mice. *Neuron* **56**, 907-923 (2007).
28. O. G. Ayling, T. C. Harrison, J. D. Boyd, A. Goroshkov, T. H. Murphy, Automated light-based mapping of motor cortex by photoactivation of channelrhodopsin-2 transgenic mice. *Nature methods* **6**, 219-224 (2009).
29. J. H. Lee *et al.*, Global and local fMRI signals driven by neurons defined optogenetically by type and wiring. *Nature* **465**, 788-792 (2010).
30. W. B. Jung, H. J. Shim, S. G. Kim, Mouse BOLD fMRI at ultrahigh field detects somatosensory networks including thalamic nuclei. *NeuroImage* **195**, 203-214 (2019).
31. M. Desai *et al.*, Mapping brain networks in awake mice using combined optical neural control and fMRI. *Journal of neurophysiology* **105**, 1393-1405 (2011).
32. X. Chen *et al.*, Sensory evoked fMRI paradigms in awake mice. *NeuroImage* **204**, 116242 (2020).

33. S. Zhao *et al.*, Cell type–specific channelrhodopsin-2 transgenic mice for optogenetic dissection of neural circuitry function. *Nature methods* **8**, 745-752 (2011).
34. F. Schlegel *et al.*, Fiber-optic implant for simultaneous fluorescence-based calcium recordings and BOLD fMRI in mice. *Nature protocols* **13**, 840-855 (2018).
35. H. J. Shim *et al.*, Mouse fMRI under ketamine and xylazine anesthesia: Robust contralateral somatosensory cortex activation in response to forepaw stimulation. *NeuroImage* **177**, 30-44 (2018).
36. B. A. Duffy, M. Choy, M. R. Chuapoco, M. Madsen, J. H. Lee, MRI compatible optrodes for simultaneous LFP and optogenetic fMRI investigation of seizure-like afterdischarges. *NeuroImage* **123**, 173-184 (2015).
37. D. Bernal-Casas, H. J. Lee, A. J. Weitz, J. H. Lee, Studying Brain Circuit Function with Dynamic Causal Modeling for Optogenetic fMRI. *Neuron* **93**, 522-532.e525 (2017).
38. S. G. Kim *et al.*, Cerebral blood volume MRI with intravascular superparamagnetic iron oxide nanoparticles. *NMR in biomedicine* **26**, 949-962 (2013).
39. H. G. Rey, C. Pedreira, R. Quian Quiroga, Past, present and future of spike sorting techniques. *Brain research bulletin* **119**, 106-117 (2015).
40. H. S. Moon *et al.*, Contribution of Excitatory and Inhibitory Neuronal Activity to BOLD fMRI. *Cerebral cortex (New York, N.Y. : 1991)* 10.1093/cercor/bhab068 (2021).
41. K. H. Pettersen, A. Devor, I. Ulbert, A. M. Dale, G. T. Einevoll, Current-source density estimation based on inversion of electrostatic forward solution: effects of finite extent of neuronal activity and conductivity discontinuities. *Journal of neuroscience methods* **154**, 116-133 (2006).
42. R. W. Cox, AFNI: software for analysis and visualization of functional magnetic resonance neuroimages. *Computers and biomedical research, an international journal* **29**, 162-173 (1996).
43. S. M. Smith *et al.*, Advances in functional and structural MR image analysis and implementation as FSL. *NeuroImage* **23 Suppl 1**, S208-219 (2004).
44. B. B. Avants *et al.*, A reproducible evaluation of ANTs similarity metric performance in brain image registration. *NeuroImage* **54**, 2033-2044 (2011).
45. W. B. Jung, G. H. Im, H. Jiang, S.-G. Kim, Early fMRI responses to somatosensory and optogenetic stimulation reflect neural information flow. *Proceedings of the National Academy of Sciences* **118**, e2023265118 (2021).
46. P. K. Mandal, R. Mahajan, I. D. Dinov, Structural brain atlases: design, rationale, and applications in normal and pathological cohorts. *Journal of Alzheimer's disease : JAD* **31 Suppl 3**, S169-188 (2012).
47. Y. Y. Shih *et al.*, Ultra high-resolution fMRI and electrophysiology of the rat primary somatosensory cortex. *NeuroImage* **73**, 113-120 (2013).

48. N. Li *et al.*, Spatiotemporal constraints on optogenetic inactivation in cortical circuits. *eLife* **8** (2019).
49. L. Lee *et al.*, Key Aspects of Neurovascular Control Mediated by Specific Populations of Inhibitory Cortical Interneurons. *Cerebral cortex (New York, N.Y. : 1991)* **30**, 2452-2464 (2020).
50. E. Jonckers, J. Van Audekerke, G. De Visscher, A. Van der Linden, M. Verhoye, Functional connectivity fMRI of the rodent brain: comparison of functional connectivity networks in rat and mouse. *PloS one* **6**, e18876 (2011).
51. J. Paasonen, P. Stenroos, R. A. Salo, V. Kiviniemi, O. Gröhn, Functional connectivity under six anesthesia protocols and the awake condition in rat brain. *NeuroImage* **172**, 9-20 (2018).
52. A. E. Mechling *et al.*, Fine-grained mapping of mouse brain functional connectivity with resting-state fMRI. *NeuroImage* **96**, 203-215 (2014).
53. F. Sforazzini, A. J. Schwarz, A. Galbusera, A. Bifone, A. Gozzi, Distributed BOLD and CBV-weighted resting-state networks in the mouse brain. *NeuroImage* **87**, 403-415 (2014).
54. F. A. Nasrallah, H. C. Tay, K. H. Chuang, Detection of functional connectivity in the resting mouse brain. *NeuroImage* **86**, 417-424 (2014).
55. W. B. Jung *et al.*, Neuroplasticity for spontaneous functional recovery after neonatal hypoxic ischemic brain injury in rats observed by functional MRI and diffusion tensor imaging. *NeuroImage* **126**, 140-150 (2016).
56. J. Grandjean, A. Schroeter, I. Batata, M. Rudin, Optimization of anesthesia protocol for resting-state fMRI in mice based on differential effects of anesthetics on functional connectivity patterns. *NeuroImage* **102 Pt 2**, 838-847 (2014).
57. R. A. Mease, A. Sumser, B. Sakmann, A. Groh, Cortical Dependence of Whisker Responses in Posterior Medial Thalamus In Vivo. *Cerebral cortex (New York, N.Y. : 1991)* **26**, 3534-3543 (2016).
58. R. A. Mease, A. Sumser, B. Sakmann, A. Groh, Corticothalamic Spike Transfer via the L5B-POm Pathway in vivo. *Cerebral cortex (New York, N.Y. : 1991)* **26**, 3461-3475 (2016).
59. M. Suzuki, M. E. Larkum, General Anesthesia Decouples Cortical Pyramidal Neurons. *Cell* **180**, 666-676.e613 (2020).
60. A. J. Keller, M. M. Roth, Feedback generates a second receptive field in neurons of the visual cortex. *Nature* **582**, 545-549 (2020).
61. J. Ni, J. L. Chen, Long-range cortical dynamics: a perspective from the mouse sensorimotor whisker system. *The European journal of neuroscience* **46**, 2315-2324 (2017).
62. A. J. Poplawsky *et al.*, Dominance of layer-specific microvessel dilation in contrast-enhanced high-resolution fMRI: Comparison between hemodynamic spread and vascular architecture with CLARITY. *NeuroImage* **197**, 657-667 (2019).
63. C. C. Liao, C. T. Yen, Functional connectivity of the secondary somatosensory cortex of the rat. *Anatomical record (Hoboken, N.J. : 2007)* **291**, 960-973 (2008).

64. B. B. Theyel, D. A. Llano, S. M. Sherman, The corticothalamocortical circuit drives higher-order cortex in the mouse. *Nature neuroscience* **13**, 84-88 (2010).
65. C. C. Lee, S. M. Sherman, Synaptic properties of thalamic and intracortical inputs to layer 4 of the first- and higher-order cortical areas in the auditory and somatosensory systems. *Journal of neurophysiology* **100**, 317-326 (2008).
66. C. C. Petersen, The functional organization of the barrel cortex. *Neuron* **56**, 339-355 (2007).
67. Z. P. Rosenthal *et al.*, Local Perturbations of Cortical Excitability Propagate Differentially Through Large-Scale Functional Networks. *Cerebral cortex (New York, N.Y. : 1991)* **30**, 3352-3369 (2020).
68. J. Seamans, Losing inhibition with ketamine. *Nature chemical biology* **4**, 91-93 (2008).
69. T. N. A. Dinh, W. B. Jung, H. J. Shim, S. G. Kim, Characteristics of fMRI responses to visual stimulation in anesthetized vs. awake mice. *NeuroImage* **226**, 117542 (2021).
70. R. Aronoff *et al.*, Long-range connectivity of mouse primary somatosensory barrel cortex. *The European journal of neuroscience* **31**, 2221-2233 (2010).
71. T. Mao *et al.*, Long-range neuronal circuits underlying the interaction between sensory and motor cortex. *Neuron* **72**, 111-123 (2011).
72. B. M. Hooks, Sensorimotor Convergence in Circuitry of the Motor Cortex. *The Neuroscientist : a review journal bringing neurobiology, neurology and psychiatry* **23**, 251-263 (2017).
73. S. E. Kwon, H. Yang, G. Minamisawa, D. H. O'Connor, Sensory and decision-related activity propagate in a cortical feedback loop during touch perception. **19**, 1243-1249 (2016).
74. H. Yang, S. E. Kwon, K. S. Severson, D. H. O'Connor, Origins of choice-related activity in mouse somatosensory cortex. **19**, 127-134 (2016).
75. T. Yamashita *et al.*, Membrane potential dynamics of neocortical projection neurons driving target-specific signals. *Neuron* **80**, 1477-1490 (2013).
76. Y. B. Saalmann, Intralaminar and medial thalamic influence on cortical synchrony, information transmission and cognition. *Frontiers in systems neuroscience* **8**, 83 (2014).